Research Article

Nano Research
2021, 14(12): 4528–4533

ISSN 1998-0124 CN 11-5974/O4
https://doi.org/10.1007/s12274-021-3366-3

Corrosion formation and phase transformation of nickel-iron hydroxide nanosheets array for efficient water oxidation

Lanqian Gong[1], Huan Yang[2], Hongming Wang[3], Ruijuan Qi[4], Junlei Wang[1], Shenghua Chen[1], Bo You[1], Zehua Dong[1], Hongfang Liu[1], and Bao Yu Xia[1] (✉)

[1] *Key laboratory of Material Chemistry for Energy Conversion and Storage (Ministry of Education), Hubei Key Laboratory of Material Chemistry and Service Failure, Wuhan National Laboratory for Optoelectronics, School of Chemistry and Chemical Engineering, Huazhong University of Science and Technology (HUST), Wuhan 430074, China*
[2] *School of Materials Science and Engineering, Wuhan Institute of Technology, Wuhan 430074, China*
[3] *Institute for Advanced Study, Nanchang University, Nanchang 330000, China*
[4] *Department of Information Science and Technology, East China Normal University, Shanghai 200240, China*

Received: 16 December 2020 / **Revised:** 26 January 2021 / **Accepted:** 27 January 2021

ABSTRACT

Designing earth-abundant electrocatalysts with high performance towards water oxidation is highly decisive for the sustainable energy technologies. This study develops a facile natural corrosion approach to fabricate nickel-iron hydroxides for water oxidation. The resulted electrode demonstrates an outstanding activity and stability with an overpotential of 275 mV to deliver 10 mA·cm^{-2}. Experimental and theoretical results suggest the corrosion-induced formation of hydroxides and their transformation to oxyhydroxides would account for this excellent performance. This work not only provides an interesting corrosion approach for the fabrication of excellent water oxidation electrode, but also bridges traditional corrosion engineering and novel materials fabrication, which would offer some insights in the innovative principles for nanomaterials and energy technologies.

KEYWORDS

water oxidation, electrocatalyst, corrosion, hydroxide, phase transformation

1 Introduction

The growing population and energy demand call for the renewable energy technologies to meet the development of sustainable society [1]. Water splitting, carbon dioxide reduction, and rechargeable metal-air batteries have attracted extensive attentions of academic and industrial communities [2–4]. However, due to the sluggish water oxidation, which involves the complicated multistep electron-coupled proton transfers, these technologies could not meet the desired efficiency [5, 6]. Hence, highly efficient electrocatalysts are required to overcome the energy barrier and accelerate their electrochemical reaction kinetics [7–9]. Currently, precious metal iridium/ruthenium-based composites are considered as highly active catalysts for improving the overall energy efficiencies of water oxidation [10, 11]. However, these disadvantages of less abundance and higher cost restrict their large-scale applications in energy conversion technologies. Therefore, earth-abundant transition-metal composites have received extensive attentions to replace precious catalysts [12–14]. In particular, Ni-Fe oxides/hydroxides have been explored in depth as the alternative electrocatalysts [15–17]. Various approaches like hydrothermal treatment and electrodeposition have been developed to achieve the synthesis of active Ni-Fe oxides/hydroxides [18, 19]. Nevertheless, these above bottom-up strategies often require strict conditions and complex process to realize the controllable assembly and construction of the nanostructured electrocatalysts. These meticulous syntheses are difficult for their large-scale fabrications. Developing facile top-down approaches to prepare Ni-Fe oxides/hydroxides is therefore imperative yet challenging.

In nature, metal corrosion is happening everywhere, which adversely affects and shortens the service life of engineering materials, leading to the failure of infrastructures with a subsequent economic loss to the human society [20]. However, from chemistry point of view, the corrosion products are often the mixture of metal (hydro)oxides, may containing sulfides, or chlorides [21, 22]. These phenomena inspire the possible preparation of transition metal composites for water oxidation. For example, treating the metal substrates in the corrosive environment like metal salts or chlorine atmosphere can achieve the formation of nanosheet array films rather than the common metal rusts [23, 24]. To this end, in contrast to the anti-corrosion and protection of engineering metal materials, we can employ the corrosion engineering and control the corrosion behaviors to prepare efficient electrodes for water oxidation.

Inspired by the natural corrosion phenomena, we report herein the preparation of Ni-Fe hydroxide and its transformation to oxyhydroxide for efficient water oxidation. The resulted Ni-Fe oxyhydroxide demonstrates an excellent oxygen evolution reaction (OER) activity, which exhibits an overpotential of only 275 mV at 10 mA·cm^{-2} with a remarkable stability at a large current density. Experimental and theoretical results reveal that the corrosion engineering determines the formation of Ni-Fe hydroxides, and the subsequent electrochemical activation

Address correspondence to byxia@hust.edu.cn

results in the transformation to Ni-Fe oxyhydroxide, which is responsible for the enhanced catalytic performance. High-efficiency catalysts can be synthesized by controlling the corrosion conditions in the corrosive environment, which has great potential in the synthesis of transition metal-based OER catalysts. The elements introduced in different corrosive environments are changeable and worthy of further exploration. This study demonstrates a facile top-down strategy by natural corrosion engineering to achieve valuable electrocatalysts, thus bridging traditional science and modern nanotechnologies, which may broaden the new interdisciplinary approach for science and technology community.

2 Experimental

2.1 Preparation of $NiFe(OH)_2$ and other contrast electrodes

Nickel foam (NF) (1 cm × 1.5 cm) was selected as the substrate in this research. NF was pretreated by ultrasonication in a mixture of acetone and anhydrous ethanol (volume ratio is 1:1) for 30 min, then ultrasonicated in 3.0 M HCl for 15 min, finally cleaned with distilled water and anhydrous ethanol for three times and dried with nitrogen gas before use. Subsequently, the electrodes were soaked in different corrosion solutions at 37 °C to obtain a series of target electrodes (Table S1 in the Electronic Supplementary Material, ESM). To confirm the decisive component on the catalytic performance, corrosion environment with different components ($(NH_4)_2SO_4$, $NaNO_3$, K_2HPO_4, $MgSO_4{\cdot}7H_2O$, $CaCl_2$, citrate acid (CA), ammonium citrate (AC), ferric citrate (FC), and ammonium ferric citrate (AFC)) was investigated. Different concentrations of AFC with 2.7, 5.4, 10.7, 16.0, and 20.5 mM were also investigated. Considering the effects of the corrosion time on the catalytic performance, different corrosion time with 1 and 5 min, 1, 5, and 24 h was studied.

2.2 Structural characterization

Scanning electron microscope (SEM, JSM-7600F, Japan) and transmission electron microscope (TEM, Tecnai G2 F30, Netherlands) were used to observe the morphologies of various electrodes. Energy-dispersive spectroscopy (EDS, Tecnai G2 F30, Netherlands) was used to determine the composition of various electrodes. X-ray photoelectron spectroscopy (XPS, VG Multilab 2000) was measured with an Al Kα (1,486.6 eV) radiation. The Raman spectrum (HR800, France) was collected at the wavelength of 532 cm^{-1}.

2.3 Electrochemical measurements.

The electrochemical measurements were performed on Autolab 302N potentiostat/galvanostat using three-electrode system at 25 °C. Graphite rod was used as the counter electrode and a saturated calomel electrode (SCE) electrode with saturated KCl salt bridge as the reference electrode. The prepared electrode was used as the working electrode. All electrochemical measurements were performed in 1.0 M KOH. The linear sweep voltammetry (LSV) curves were recorded from 1.0 to 1.8 V vs. reversible hydrogen electrode (RHE) at a scan rate of 2.0 $mV{\cdot}s^{-1}$. Potentials are converted using the following formula: $E_{(RHE)} = E_{(SCE)} + 0.0591 \times pH + 0.24$. The electrochemical impedance spectroscopy (EIS) was measured at the potential of 1.54 V vs. RHE with the frequency range 10^5–0.01 Hz, and the internal resistance of solution (R_S) was applied to iR-compensation during LSV tests. Cyclic voltammetry (CV) measurements were tested from 1.07 to 1.18 V vs. RHE at the scan rates of 20, 50, 100, 150, 200, and 250 $mV{\cdot}s^{-1}$. The electrochemical stability was tested at different constant current densities of 10, 50, and 100 $mA{\cdot}cm^{-2}$. All tests were repeated at least three times to ensure the reliability of the results.

2.4 Computational methods

The entire data of density functional theory (DFT) calculations were performed with the plane-wave code Vienna *ab-initio* simulation package (VASP). The details are presented in the ESM.

3 Results and discussion

The preparation of Ni-Fe hydroxides was swiftly accomplished by simply soaking NF in a mimetic natural environment for several minutes. As the corrosion time increases in the AFC-containing solution, the surface color of the electrode gradually changes from grey to dark grey (Fig. S1 in the ESM). SEM image reveals that the corrosion products, the nanosheet array, are uniformly coated on the NF surface (Fig. 1(a)). TEM observation further verifies the fluffy nanosheets with lamellar structure (Fig. 1(b)). In the enlarged TEM image, the thickness of nanosheet exhibits as ~ 5 nm (Fig. 1(c)). Furthermore, a closer high-resolution TEM(HRTEM) observation in Fig. 1(d) displays the lattice spacing of 0.25 nm, coincidentally corresponding to the (111) plane of α-$Ni(OH)_2$ [25, 26]. The high-angle annular dark field (HAADF)-scanning transmission electron microscopy (STEM) and EDS present the uniform distribution of Ni, Fe, and O elements in the nanosheets, indicating the homogeneous formation of Ni-Fe hydroxide during the corrosion process (Fig. 1(e) and Fig. S2 in the ESM).

Prior to electrochemical measurement, the electrodes are usually cleaned and activated by simple CV method. This process may result in the microstructure evolution, but most researches often ignore or fail to notice the essential phase transformation brought by this electrochemical activation. We firstly employed SEM observation to analyze the morphology evolution after a short activation (Fig. 2(a)). As shown in Fig. 2(a), corrosion product remains in similar nanosheet array morphology after a short CV process. However, further TEM observation reveals

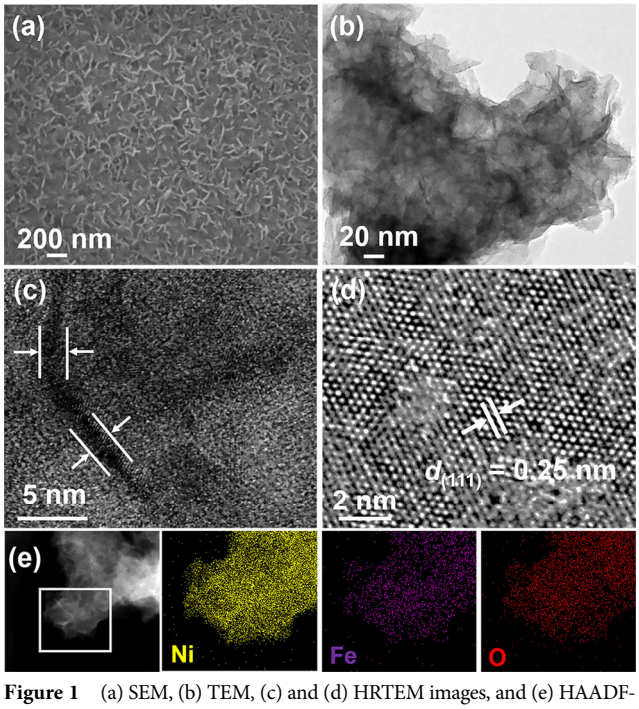

Figure 1 (a) SEM, (b) TEM, (c) and (d) HRTEM images, and (e) HAADF-STEM image and corresponding element mapping of $Ni(Fe)(OH)_2$.

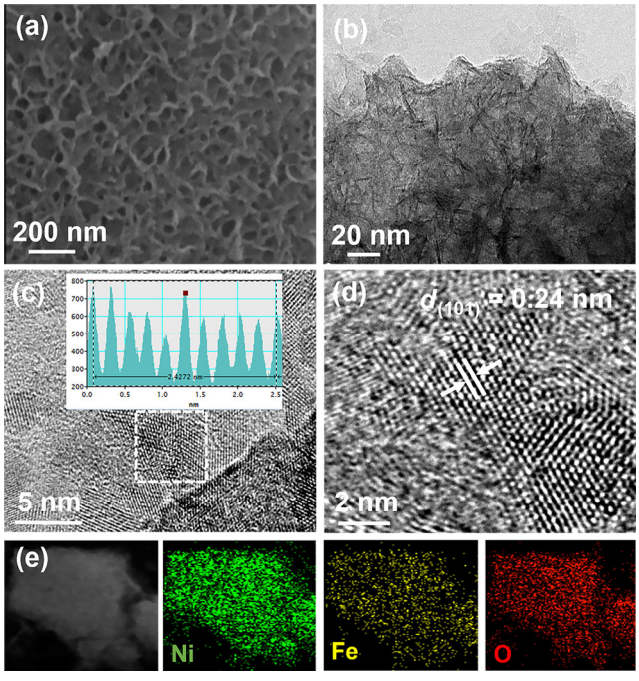

Figure 2 (a) SEM, (b) TEM, (c) and (d) HRTEM images, and (e) STEM and corresponding element mapping of Ni(Fe)OOH. The inset figure in (c) is lattice measurement result.

some roughness in the nanosheets surface (Fig. 2(b)). HRTEM images clearly demonstrate the structure transition, as the disordered nanosheets with abundant edges, pore, and defects appear in the activated sample (Fig. 2(c)). Especially, the lattice distance of 0.24 nm corresponds to the (101) plane of α-NiOOH (Fig. 2(d) and Fig. S3 in the ESM). The above results verify the transformation of α-Ni(Fe)$(OH)_2$ to α-Ni(Fe)OOH even after a short activation process, which is mainly involved in the fast subtraction of protons during the oxidation of Ni-Fe hydroxide nanosheets [27]. Furthermore, the STEM image and EDS mapping results also verify the Fe, Ni, and O elements are uniformly dispersed even after the activation and phase transition (Fig. 2(e) and Fig. S4 in the ESM).

Raman spectroscopy was further employed to assess the corrosion products and the phase transformation induced by electrochemical activation. Raman spectrum of corrosion products shows two peaks at ~ 475 and 530 cm^{-1}, which are attributed to the stretching modes of Ni–OH and Ni–O in the Ni(Fe)$(OH)_2$, respectively [28, 29]. However, the former peak at 475 cm^{-1} for Ni–OH is obviously weakened while the later at 530 cm^{-1} for Ni–O is enhanced after the activation, which suggests the corrosion products of Ni(Fe)$(OH)_2$ have suffered from the phase transformation from hydroxide to oxyhydroxides (Fig. 3(a)). In the full XPS, the coexistence of O, Ni, and Fe is further clarified in the as-obtained corrosion products (Fig. S5 in the ESM). The Ni 2p signal occupies a pair of dominant positions at 854.0 and 871.6 eV, matching with Ni $2p_{1/2}$ and Ni $2p_{3/2}$, along with two less intense satellite peaks, which indicate the presence of Ni(II) components in the Ni(Fe)$(OH)_2$ and Ni(Fe)OOH (Fig. 3(b)). However, the emerged peaks at 857.1 and 874.8 eV are observed for the Ni(III) species in the Ni(Fe)OOH spectrum, which verifies again the transformation of hydroxides to oxyhydroxides in the corrosion electrode [30, 31]. Moreover, the O 1s spectra reveal three oxygen contributions (Fig. 3(c)), which are assigned to the O–H (532.8 eV), M (Ni, Fe)–OH (531.3 eV) and M (Ni, Fe)–O (530.0 eV) species [32]. After a short activation, the produced Ni(Fe)OOH shows an increased area of M–O and a decreased area of M–OH. The ratios of M–O and M–OH bonds increase from 89.7 to 91.5% after the activation, which further indicates the transformation of hydroxides to oxyhydroxides. Moreover, the Fe 2p XPS spectra of Ni(Fe)$(OH)_2$ and Ni(Fe)OOH samples possess the similar major peaks at 725.0 and 712.3 eV, which are identified as Fe(III) species (Fig. 3(d)) [33].

Figure 4(a) shows CV peaks at ~ 1.36 and 1.50 V vs. RHE,

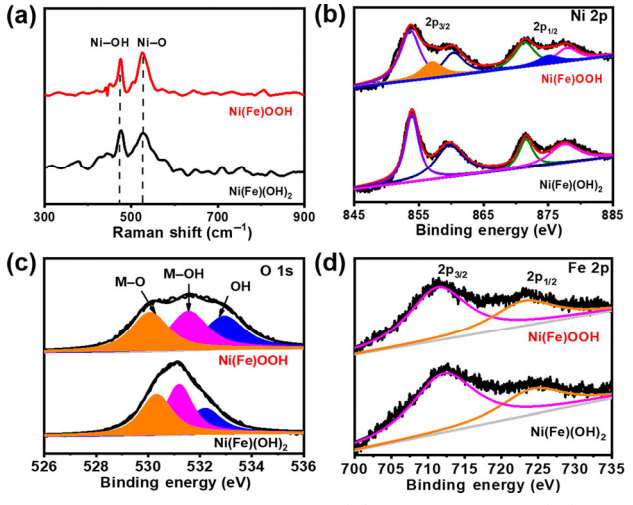

Figure 3 (a) Raman survey spectra, and (b) Ni 2p, (c) O 1s, and (d) Fe 2p XPS analysis of Ni(Fe)$(OH)_2$ and Ni(Fe)OOH.

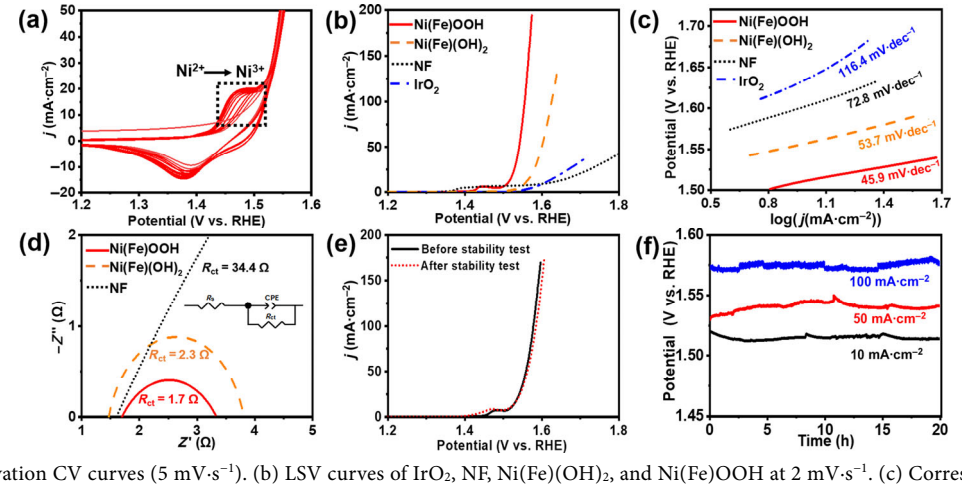

Figure 4 (a) Activation CV curves (5 mV·s^{-1}). (b) LSV curves of IrO_2, NF, Ni(Fe)$(OH)_2$, and Ni(Fe)OOH at 2 mV·s^{-1}. (c) Corresponding Tafel plots. (d) EIS curves (measured at 1.54 V vs. RHE). (e) LSV curves of Ni(Fe)OOH before and after stability tests (2 mV·s^{-1}), and (f) stability test at 10, 50, and 100 mA·cm^{-2} of Ni(Fe)OOH. All electrochemical data are collected in 1.0 M KOH.

which are associated to the redox of Ni(II)/Ni(III) pair [34]. The phase transition of $Ni(Fe)(OH)_2$ to Ni(Fe)OOH is quickly completed in a few cycles (ca. 10 cycles) (Fig. S6 in the ESM). Notably, the activated Ni(Fe)OOH electrode requires an overpotential of 275 mV to inspire 10 $mA{\cdot}cm^{-2}$ current density (Fig. 4(b)), overpassing by 50 mV than the fresh $Ni(Fe)(OH)_2$. Compared with the benchmarked IrO_2 catalyst and NF substrate, the overpotential of Ni(Fe)OOH also negatively shifts 100 and 110 mV, respectively. The property of Ni(Fe)OOH is comparable with that of NiFe-based materials synthesized by different methods (Table S2 in the ESM). Moreover, the corresponding Tafel slopes reveal an identical tendency for the enhanced performance (Fig. 4(c)). The Tafel slope of 45.9 $mV{\cdot}dec^{-1}$ for the activated Ni(Fe)OOH electrode is better than that of the fresh $Ni(Fe)(OH)_2$ (53.7 $mV{\cdot}dec^{-1}$), NF substrate (72.8 $mV{\cdot}dec^{-1}$), and commercial IrO_2 (116.4 $mV{\cdot}dec^{-1}$), indicating the favorable kinetics of Ni(Fe)OOH electrode. The electrochemical double layer capacitances (C_{dl}) were then performed to compare the electrochemical surface areas (ECSA) of different materials. Compared with NF substrate (1.9 $mF{\cdot}cm^{-2}$), the resulted Ni(Fe)OOH shows higher C_{dl} (2.6 $mF{\cdot}cm^{-2}$) and ECSA, illustrating the corrosion-generated electrode with abundant nanosheets array on the NF substrate would increase the density of active sites. After the ECSA correction, the Ni(Fe)OOH electrode still demonstrates a higher current density over all potential range (Fig. S7 in the ESM), this could be speculated by the high intrinsic activity of Ni(Fe)OOH derived from the corrosion layer. To further investigate the interfacial charge-transfer capability during the electrochemical reaction, the EIS at 1.54 V vs. RHE was carried out (Fig. 4(d)). Compared with the fresh $Ni(Fe)(OH)_2$ electrode (~ 2.3 Ω) and NF substrate (~ 34.4 Ω), the charge-transfer resistance (R_{ct}) of ~ 1.7 Ω for the activated Ni(Fe)OOH electrode is much smaller. This result implies that the formed active corrosion layer is beneficial for the interfacial contact, the transformation of hydroxide to oxyhydroxide further enhances the interfacial charge transfer and contributes to the improved activity. The Faradaic efficiency (FE) of oxygen production was further monitored, where a high FE of 98% demonstrates water oxidation over the Ni(Fe)OOH electrode is mainly dominated by the oxygen production (Fig. S8 in the ESM). Finally, no conspicuous activity loss is observed during the extensive periodic stability measurements at 10, 50, and 100 $mA{\cdot}cm^{-2}$, further identifying the salient stability and practical feasibility (Figs. 4(e) and 4(f)). After the stability test, the electrode surface still maintains a relatively loose nanosheet structure (Fig. S9 in the ESM).

As our corrosion experiments are simulated from the natural corrosion environment, we then investigated the environment conditions to reveal the corrosive effect on the electrocatalytic process. Different corrosion time, active substances, and concentration were successively discussed. Among different components in the corrosive environment, the best electrode is achieved in the AFC solution and the other environmental components are almost not helpful in improving the activity (Fig. S10 in the ESM). Furthermore, more experiments of different corrosion-formed electrodes show the Fe ions are decisive to improve the catalytic activity (Fig. S11 in the ESM). The corrosion-formed $Ni(Fe)(OH)_2$ is mainly related to the oxidation corrosion of NF, owning to the rich hydroxyl at local corrosion place ($Ni + Fe(III) + 2OH^- = Ni(Fe)(OH)_2$). With the increase of concentration of Fe ions, the activity of corrosion-formed electrode firstly increases and then remains stable after achieving an optimum activity at 5.4 mM Fe(III) ions (Fig. S12 in the ESM). This is mainly attributed to the optimal surface morphology as more Fe ions would result in more compact corrosion layer, which would destroy the porous array structure (Fig. S13 in the ESM). Moreover, with the increase of corrosion time, the catalytic performance of corrosion-formed electrode increases initially and then keeps almost the same (Fig. S14 in the ESM). Notably, after one-minute corrosion time, the overpotential of corrosion electrode is 310 mV, and the overpotential reduces to 280 mV after 5 h corrosion, indicating efficient electrodes can be quickly obtained by this facile corrosion-inspired strategy.

DFT calculations were performed to investigate the water oxidation mechanism of corrosion electrodes. The structures of Fe-incorporated NiOOH were constructed and the computations were performed on the Fe-on-top sites (Fig. 5(a)) [35]. Compared with the structure of $Ni(OH)_2$, part of the Fe atoms in the $Ni(Fe)(OH)_2$ replace the Ni seat. It will go through the four-step mechanism for oxygen molecular formation, producing active intermediates of *OH, *O, and *OOH (Fig. 5(b)). Free energy gap required to generate both two intermediates can reflect the catalytic activity of electrocatalysts, i.e. $\Delta G_{*OH} - \Delta G_{*O}$, $\Delta G_{*O} - \Delta G_{*OOH}$ [36, 37]. The surface oxidation occurs on the $Ni(OH)_2$ during the electrochemical activation process, and a lower free energy gap from *OH to *O and *O to *OOH will lead to a reduced overpotential of NiOOH (0.5) than that of the corresponding $Ni(OH)_2$ (0.85) (Fig. 5c), implying the oxygen evolution catalyzed by NiOOH is more favorable than $Ni(OH)_2$. After the incorporation of Fe, the transformation from *OH to *O is the rate-determining step (Fig. S15 and Table S3 in the ESM). Moreover, the incorporation of Fe will induce a decreased free energy gap between *O and *OOH, leading to a reduced overpotential for $Ni(Fe)(OH)_2$ and Ni(Fe)OOH. Compared with $Ni(Fe)(OH)_2$, a lower adsorption and desorption energy of reaction intermediate of Ni(Fe)OOH evidently strengthen the electrocatalytic activity. Upon the incorporation of Fe atoms, the total density of states (DOS) around the Fermi level for Ni(Fe)OOH display a significant enhancement compared with that of NiOOH (Fig. 5(d)). More spin-down states of electrons appear and effectively modulate the electron occupancy, which is likely caused by less electrons in d-orbital of Fe atoms ($3d^6 4s^2$) [38]. Such variation would give rise to the d-band center shift closer to the Fermi level, which is more favorable for the adsorption/desorption of oxygen-containing groups [39].

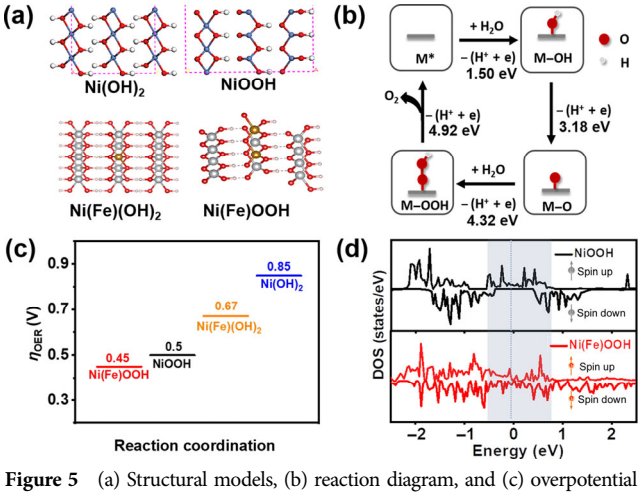

Figure 5 (a) Structural models, (b) reaction diagram, and (c) overpotential calculation of Ni(Fe)OOH, NiOOH, $Ni(Fe)(OH)_2$, and $Ni(OH)_2$, and (d) total DOS profiles of NiOOH and Ni(Fe)OOH.

4 Conclusions

In summary, we report the preparation of hydroxides and its transformation to oxyhydroxides for the efficient water oxidation. The resulted Ni(Fe)OOH requires an overpotential of only

275 mV to reach 10 mA·cm^{-2}, which shows the remarkable stability at large current densities. Experimental and theoretical results indicate that the corrosion engineering induces the formation of Ni(Fe)$(OH)_2$, the subsequent electrochemical activation results in the transformation to Ni(Fe)OOH. The electrodes formed through corrosion approach show the decreased adsorption and desorption energies of reaction intermediates, which are responsible for the improved catalytic performance. This work demonstrates a top-down strategy by corrosion engineering to achieve valuable nanomaterials, which bridges the traditional engineering and modern nanotechnologies, thus likely to broaden the new interdisciplinary for science and technology community.

Acknowledgements

This work is financially supported by the National Natural Science Foundation of China (No. 22075092), China Postdoctoral Science Foundation (No. 2018M642810), and the Program for HUST Academic Frontier Youth Team (No. 2018QYTD15). We also acknowledge the support of Analytical and Testing Center of Huazhong University of Science and Technology for Raman, SEM, and TEM measurements.

Electronic Supplementary Material: Supplementary material (DFT calculation methods; supplementary figures and tables) is available in the online version of this article at https://doi.org/10.1007/s12274-021-3366-3.

References

[1] Montoya, J. H.; Seitz, L. C.; Chakthranont, P.; Vojvodic, A.; Jaramillo, T. F.; Nørskov, J. K. Materials for solar fuels and chemicals. *Nat. Mater.* **2017**, *16*, 70–81.

[2] Chen, R.; Hung, S. F.; Zhou, D. J.; Gao, J. J.; Yang, C. J.; Tao, H. B.; Yang, H. B.; Zhang, L. P.; Zhang, L. L.; Xiong, Q. H. et al. Layered structure causes bulk NiFe layered double hydroxide unstable in alkaline oxygen evolution reaction. *Adv. Mater.* **2019**, *31*, 1903909.

[3] Fang, W. S.; Huang, L.; Zaman, S.; Wang, Z. T.; Han, Y. J.; Xia, B. Y. Recent progress on two-dimensional electrocatalysis. *Chem. Res. Chin. Univ.* **2020**, *36*, 611–621.

[4] Xu, Y. Y.; Deng, P. L.; Chen, G. D.; Chen, J. X.; Yan, Y.; Qi, K.; Liu, H. F.; Xia, B. Y. 2D nitrogen-doped carbon nanotubes/graphene hybrid as bifunctional oxygen electrocatalyst for long-life rechargeable Zn–air batteries. *Adv. Funct. Mater.* **2020**, *30*, 1906081.

[5] Gong, L. Q.; Yang, H.; Douka, A. I.; Yan, Y.; Xia, B. Y. Recent progress on NiFe-based electrocatalysts for alkaline oxygen evolution. *Adv. Sustain. Syst.* **2021**, *5*, 2000136.

[6] Jiao, Y.; Zheng, Y.; Jaroniec, M.; Qiao, S. Z. Design of electrocatalysts for oxygen- and hydrogen-involving energy conversion reactions. *Chem. Soc. Rev.* **2015**, *44*, 2060–2086.

[7] Liao, P. L.; Keith, J. A.; Carter, E. A. Water oxidation on pure and doped hematite (0001) surfaces: Prediction of Co and Ni as effective dopants for electrocatalysis. *J. Am. Chem. Soc.* **2012**, *134*, 13296–13309.

[8] Dotan, H.; Landman, A.; Sheehan, S. W.; Malviya, K. D.; Shter, G. E.; Grave, D. A.; Arzi, Z.; Yehudai, N.; Halabi, M.; Gal, N. et al. Decoupled hydrogen and oxygen evolution by a two-step electrochemical–chemical cycle for efficient overall water splitting. *Nat. Energy* **2019**, *4*, 786–795.

[9] Roger, I.; Shipman, M. A.; Symes, M. D. Earth-abundant catalysts for electrochemical and photoelectrochemical water splitting. *Nat. Rev. Chem.* **2017**, *1*, 0003.

[10] Zhang, J. Y.; Yan, Y.; Mei, B. B.; Qi, R. J.; He, T.; Wang, Z. T.; Fang, W. S.; Zaman, S.; Su, Y. Q., Ding, S. J. et al. Local spin-state tuning of cobalt-iron selenide nanoframes for the boosted oxygen evolution. *Energy Environ. Sci.* **2021**, *14*, 365–373.

[11] Lee, Y.; Suntivich, J.; May, K. J.; Perry, E. E.; Shao-Horn, Y. Synthesis and activities of rutile IrO_2 and RuO_2 nanoparticles for oxygen evolution in acid and alkaline solutions. *J. Phys. Chem. Lett.* **2012**, *3*, 399–404.

[12] Sun, D.; Shen, Y.; Zhang, W.; Yu, L.; Yi, Z. Q.; Yin, W.; Wang, D.; Huang, Y. H.; Wang, J.; Wang, D. L. et al. A solution-phase bifunctional catalyst for lithium–oxygen batteries. *J. Am. Chem. Soc.* **2014**, *136*, 8941–8946.

[13] Subbaraman, R.; Tripkovic, D.; Chang, K. C.; Strmcnik, D.; Paulikas, A. P.; Hirunsit, P.; Chan, M.; Greeley, J.; Stamenkovic, V.; Markovic, N. M. Trends in activity for the water electrolyser reactions on 3*d* M(Ni, Co, Fe, Mn) hydr(oxy)oxide catalysts. *Nat. Mater.* **2012**, *11*, 550–557.

[14] Zhang, B.; Xiao, C. H.; Xie, S. M.; Liang, J.; Chen, X.; Tang, Y. H. Iron–nickel nitride nanostructures *in situ* grown on surface-redox-etching nickel foam: Efficient and ultrasustainable electrocatalysts for overall water splitting. *Chem. Mater.* **2016**, *28*, 6934–6941.

[15] Mohammed-Ibrahim, J. A review on NiFe-based electrocatalysts for efficient alkaline oxygen evolution reaction. *J. Power Sources* **2020**, *448*, 227375.

[16] Chen, G.; Zhu, Y. P.; Chen, H. M.; Hu, Z. W.; Hung, S. F.; Ma, N. N.; Dai, J.; Lin, H. J.; Chen, C. T.; Zhou, W. et al. An amorphous nickel-iron-based electrocatalyst with unusual local structures for ultrafast oxygen evolution reaction. *Adv. Mater.* **2019**, *31*, 1900883.

[17] Ma, Y. M.; Wang, K.; Liu, D. Y.; Yang, X. X.; Wu, H.; Xiao, C. H.; Ding, S. J. Surface dual-oxidation induced metallic copper doping into NiFe electrodes for electrocatalytic water oxidation. *J. Mater. Chem. A* **2019**, *7*, 22889–22897.

[18] Yin, S. M.; Tu, W. G.; Sheng, Y.; Du, Y. H.; Kraft, M.; Borgna, A.; Xu, R. A highly efficient oxygen evolution catalyst consisting of interconnected nickel-iron-layered double hydroxide and carbon nanodomains. *Adv. Mater.* **2018**, *30*, 1705106.

[19] Zhang, W.; Wu, Y. Z.; Qi, J.; Chen, M. X.; Cao, R. A thin NiFe hydroxide film formed by stepwise electrodeposition strategy with significantly improved catalytic water oxidation efficiency. *Adv. Energy Mater.* **2017**, *7*, 1602547.

[20] Lu, Z. Y.; Qian, L.; Tian, Y.; Li, Y. P.; Sun, X. M.; Duan, X. Ternary NiFeMn layered double hydroxides as highly-efficient oxygen evolution catalysts. *Chem. Commun.* **2016**, *52*, 908–911.

[21] Liu, H. W.; Fu, C. Y.; Gu, T. Y.; Zhang, G. A.; Lv, Y. L.; Wang, H. T.; Liu, H. F. Corrosion behavior of carbon steel in the presence of sulfate reducing bacteria and iron oxidizing bacteria cultured in oilfield produced water. *Corros. Sci.* **2015**, *100*, 484–495.

[22] Santana Rodríguez, J. J.; Santana Hernández, F. J.; González González, J. E. Comparative study of the behaviour of AISI 304 SS in a natural seawater hopper, in sterile media and with SRB using electrochemical techniques and SEM. *Corros. Sci.* **2006**, *48*, 1265–1278.

[23] Yin, H. J.; Jiang, L. X.; Liu, P. R.; Al-Mamun, M.; Wang, Y.; Zhong, Y. L.; Yang, H. G.; Wang, D.; Tang, Z. Y.; Zhao, H. J. Remarkably enhanced water splitting activity of nickel foam due to simple immersion in a ferric nitrate solution. *Nano Res.* **2018**, *11*, 3959–3971.

[24] Liu, Y. P.; Liang, X.; Gu, L.; Zhang, Y.; Li, G. D.; Zou, X. X.; Chen, J. S. Corrosion engineering towards efficient oxygen evolution electrodes with stable catalytic activity for over 6000 hours. *Nat. Commun.* **2018**, *9*, 2609.

[25] Liang, H. F.; Gandi, A. N.; Xia, C.; Hedhili, M. N.; Anjum, D. H.; Schwingenschlögl, U.; Alshareef, H. N. Amorphous NiFe-OH/NiFeP electrocatalyst fabricated at low temperature for water oxidation applications. *ACS Energy Lett.* **2017**, *2*, 1035–1042.

[26] Wang, J. Y.; Ji, L. L.; Zuo, S. S.; Chen, Z. F. Hierarchically structured 3D integrated electrodes by galvanic replacement reaction for highly efficient water splitting. *Adv. Energy Mater.* **2017**, *7*, 1700107.

[27] Malara, F.; Minguzzi, A.; Marelli, M.; Morandi, S.; Psaro, R.; Dal Santo, V.; Naldoni, A. α-Fe_2O_3/NiOOH: An effective heterostructure for photoelectrochemical water oxidation. *ACS Catal.* **2015**, *5*, 5292–5300.

[28] Li, H. B.; Yu, M. H.; Wang, F. X.; Liu, P.; Liang, Y.; Xiao, J.; Wang, C. X.; Tong, Y. X.; Yang, G. W. Amorphous nickel hydroxide nanospheres with ultrahigh capacitance and energy density as electrochemical pseudocapacitor materials. *Nat. Commun.* **2013**, *4*, 1894.

[29] Hunter, B. M.; Blakemore, J. D.; Deimund, M.; Gray, H. B.; Winkler, J. R.; Muller, A. M. Highly active mixed-metal nanosheet water oxidation catalysts made by pulsed-laser ablation in liquids. *J.*

Am. *Chem*. *Soc*. **2014**, *136*, 13118–13121.

[30] Gao, Y. Q.; Li, H. B.; Yang, G. W. Amorphous nickel hydroxide nanosheets with ultrahigh activity and super-long-term cycle stability as advanced water oxidation catalysts. *Cryst*. *Growth*. *Des*. **2015**, *15*, 4475–4483.

[31] Huang, J. W.; Sun, Y. H.; Zhang, Y. D.; Zou, G. F.; Yan, C. Y.; Cong, S.; Lei, T. Y.; Dai, X.; Guo, J.; Lu, R. F. et al. A new member of electrocatalysts based on nickel metaphosphate nanocrystals for efficient water oxidation. *Adv*. *Mater*. **2018**, *30*, 1705045.

[32] Yang, H.; Gong, L. Q.; Wang, H. M.; Dong, C. L.; Wang, J. L.; Qi, K.; Liu, H. F.; Guo, X. P.; Xia, B. Y. Preparation of nickel-iron hydroxides by microorganism corrosion for efficient oxygen evolution. *Nat*. *Commun*. **2020**, *11*, 5075.

[33] Xiao, C. H.; Zhang, B.; Li, D. Partial-sacrificial-template synthesis of Fe/Ni phosphides on Ni foam: A strongly stabilized and efficient catalyst for electrochemical water splitting. *Electrochim*. *Acta* **2017**, *242*, 260–267.

[34] Görlin, M.; de Araújo, J. F.; Schmies, H.; Bernsmeier, D.; Dresp, S.; Gliech, M.; Jusys, Z.; Chernev, P.; Kraehnert, R.; Dau, H. et al. Tracking catalyst redox states and reaction dynamics in Ni-Fe oxyhydroxide oxygen evolution reaction electrocatalysts: The role of catalyst support and electrolyte pH. *J*. *Am*. *Chem*. *Soc*. **2017**, *139*, 2070–2082.

[35] Friebel, D.; Louie, M. W.; Bajdich, M.; Sanwald, K. E.; Cai, Y.; Wise, A. M.; Cheng, M. J.; Sokaras, D.; Weng, T. C.; Alonso-Mori, R. et al. Identification of highly active Fe sites in (Ni, Fe)OOH for electrocatalytic water splitting. *J*. *Am*. *Chem*. *Soc*. **2015**, *137*, 1305–1313.

[36] Zhang, J. F.; Liu, J. Y.; Xi, L. F.; Yu, Y. F.; Chen, N.; Sun, S. H.; Wang, W. C.; Lange, K. M.; Zhang, B. Single-atom Au/NiFe layered double hydroxide electrocatalyst: Probing the origin of activity for oxygen evolution reaction. *J*. *Am*. *Chem*. *Soc*. **2018**, *140*, 3876–3879.

[37] Wang, T. Y.; Nam, G.; Jin, Y.; Wang, X. Y.; Ren, P. J.; Kim, M. G.; Liang, J. S.; Wen, X. D.; Jang, H.; Han, J. T. et al. NiFe (oxy)hydroxides derived from NiFe disulfides as an efficient oxygen evolution catalyst for rechargeable Zn-air batteries: The effect of surface S residues. *Adv*. *Mater*. **2018**, *30*, 1800757.

[38] Li, P. S.; Duan, X. X.; Kuang, Y.; Li, Y. P.; Zhang, G. X.; Liu, W.; Sun, X. M. Tuning electronic structure of NiFe layered double hydroxides with vanadium doping toward high efficient electrocatalytic water oxidation. *Adv*. *Energy Mater*. **2018**, *8*, 1703341.

[39] Jiang, J.; Sun, F. F.; Zhou, S.; Hu, W.; Zhang, H.; Dong, J. C.; Jiang, Z.; Zhao, J. J.; Li, J. F.; Yan, W. S. et al. Atomic-level insight into super-efficient electrocatalytic oxygen evolution on iron and vanadium co-doped nickel (oxy)hydroxide. *Nat*. *Commun*. **2018**, *9*, 2885.